● *Original Contribution*

ULTRASONIC VASCULAR VECTOR FLOW MAPPING FOR 2-D FLOW ESTIMATION

REI ASAMI,* TOMOHIKO TANAKA,* MOTOCHIKA SHIMIZU,* YOSHINORI SEKI,[†] TOMOHIDE NISHIYAMA,[†]
HAJIME SAKASHITA,[†] and TAKASHI OKADA[†]

* Research & Development Group, Hitachi, Ltd., Tokyo, Japan; and [†] Healthcare Business Unit, Hitachi, Ltd., Tokyo, Japan

Abstract—A vascular vector flow mapping (VFM) method visualizes 2-D cardiac flow dynamics by estimating the radial component of flow from the Doppler velocities and wall motion velocities using the mass conservation equation. Although VFM provides 2-D flow, the algorithm is applicable only to bounded regions. Here, a modified VFM algorithm, vascular VFM, is proposed so that the velocities are estimated regardless of the flow geometry. To validate the algorithm, a phantom mimicking a carotid artery was fabricated and VFM velocities were compared with optical particle image velocimetry (PIV) data acquired in the same imaged plane. The validation results indicate that given optimal beam angle condition, VFM velocitiy is fairly accurate, where the correlation coefficient *R* between VFM and PIV velocities is 0.95. The standard deviation of the total VFM error, normalized by the maximum velocity, ranged from 8.1% to 16.3%, whereas the standard deviation of the measured input errors ranged from 8.9% to 12.7% for color flow mapping and from 4.5% to 5.9% for subbeam calculation. These results indicate that vascular VFM is reliable as its accuracy is comparable to that of conventional Doppler-flow images. (E-mail: tomohiko.tanaka.nx@hitachi.com)   © 2019 The Author(s). Published by Elsevier Inc. on behalf of World Federation for Ultrasound in Medicine & Biology. This is an open access article under the CC BY-NC-ND license. (http://creativecommons.org/licenses/by-nc-nd/4.0/).

Key Words: Doppler ultrasound, Blood flow, Vector mapping, Carotid artery.

INTRODUCTION

Understanding the 2-D flow patterns in the vasculature may be of great clinical importance, and an emerging interest is exploring novel ways of using ultrasound to quantitatively assess complex hemodynamic patterns under different pathologic conditions such as stenosis and plaque ulceration (Jensen et al. 2016; Posada et al. 2016). Hemodynamic parameters derived from a flow pattern enable highly atherosclerosis-susceptible endothelium to be distinguished from atherosclerosis-resistant endothelium (Gimbrone and Garcia-Cardena 2013). Wall shear stress is reported to be a parameter especially relatable to vascular characteristics, and its relationships to inflammation, endothelium cellular apoptosis, plaque formation and rupture have been reported (Muth et al. 2011; Ridger et al. 2008). To diagnose beyond the morphology of the vasculature, accurate measurement of complex hemodynamic patterns of the vasculature based on 2 (or 3)-dimensional flow patterns is inevitable.

However, conventional color Doppler echocardiography only provides flow speed projected parallel to the direction of the ultrasound beam (Namekawa et al. 1983) and fails to measure the 3-D nature of the vasculature.

Several echocardiographic and vascular 2-D flow measurement methods have recently been reported (Jensen et al. 2016; Kim et al. 2004; Posada et al. 2016; Sengupta et al. 2012). We have previously reported a vector flow mapping (VFM) method (Itatani et al. 2013) that utilizes color Doppler velocities and tissue-tracking information of the cardiac wall to estimate the velocities of lateral directional flow by using the mass conservation equation assuming a planar flow (Garcia et al. 2010; Ohtsuki and Tanaka 2006). With VFM, the vortex formation and recirculation pattern in the left ventricle are visualized by using a readily available conventional ultrasound scanner without a contrast agent. By use of a left ventricular phantom with realistic 3-D flow, the VFM method has been found to be reasonably accurate (Asami et al. 2017), and its clinical applications has been studied (Nogami et al. 2013; Ro et al. 2014). By extending VFM to vascular applications, 2-D vascular flows can be visualized without using a specially

Address correspondence to: Tomohiko Tanaka, 1-280 Higashi-Koigakubo, Kokubunji, Tokyo, Japan. E-mail: tomohiko.tanaka.nx@hitachi.com

designed scanner. The conventional VFM method is applied to the left ventricle, and the flow of interest is in a cavity surrounded by the walls. In contrast, vascular flow—carotid arteries, in particular—is conventionally scanned with a linear probe parallel to the flow, and the flow of interest is usually open-ended. The difference in ventricular and vascular geometries affects boundary conditions, and the VFM algorithm must be modified to accommodate this difference.

Here we describe our proposed novel VFM method called "vascular VFM" that is suitable for vascular applications. To assess the accuracy of the proposed vascular VFM, an optically and acoustically measurable phantom modeling carotid artery (CA) was established. Using the phantom, we determined the optimal measurement conditions for vascular VFM and thoroughly investigated the accuracy of vascular VFM under optimal conditions with a comprehensive validation scheme.

VFM algorithm customized for vessels

The derivation of conventional VFM is detailed in previous reports (Asami et al. 2017; Tanaka et al. 2012; Uejima et al. 2010). Briefly, conventional VFM assumes a 2-D flow and calculates velocities by successively integrating the mass conservation equation in the lateral direction with the boundary wall velocity acquired by tissue tracking. In the case of vascular applications, in particular, carotid arteries, a linear probe is positioned typically parallel to the vessel wall, and a Doppler beam is steered at a designated steering angle, θ, for color flow mapping (CFM), as schematically illustrated in Figure 1a. With the Doppler steering, the linear probe measures Doppler velocity in tilted Cartesian coordinates with steering angle θ, where x, y and z denote the CFM coordinate system in the transverse, depth and elevation directions, respectively. The corresponding velocities are u, v and w, respectively. The continuity equation is

$$\partial_x u + \partial_y v + \partial_z w = 0 . \qquad (1)$$

If a planar flow is assumed, $\partial_z w$ equals to zero.

As illustrated in Figure 1, either the anterior or posterior wall can be used as a boundary condition. Under the no-slip condition, the boundary condition is equivalent to the cardiac wall velocities measured by tissue tracking. Depending on which vascular wall is used, eqn (1) can be integrated with respect to u and rewritten as

$$u^{\text{ord}}(x,y) = u_a(y) - \int_{x_a}^{x} \partial_y v(x,y)dx \qquad (2)$$

or

$$u^{\text{inv}}(x,y) = u_p(y) + \int_{x}^{x_p} \partial_y v(x,y)dx \qquad (3)$$

where the integral consists of depth velocity v (which can be obtained from CFM velocities), subscripts 'a' and 'p' denote the boundary conditions (BCs) on the anterior and posterior walls of the CA and superscripts "ord" and "inv" denote the calculation pathways. The fundamental difference between the left ventricle and the CA when applying the mass conservation equation is that the region of interest is not necessarily always surrounded by walls. According to the geometric relationship between a linear probe, Doppler steer angle and vessels, some areas might have one boundary condition while others might have two or none at all. The absence of BCs for certain areas, as marked by diagonal patterns in Figure 1a, is a critical issue.

To resolve the aforementioned issue, a third boundary condition is set. That is, a single Doppler beam, steered at an angle different from that used for CFM and referred to as a "subbeam," is transmitted and received, as schematically illustrated in Figure 1b, so that it crosses most of the CFM Doppler beams. At points where the CFM Doppler beam and the subbeam cross, the 2-D flow velocity is calculated and used as the third boundary condition, given by (Fox 1978)

$$
\begin{aligned}
u &= v_b \sin(\theta - \psi) \\
v_b &= \frac{v}{\cos\theta\cos\psi + \sin\theta\sin\psi} \\
\tan\psi &= -\frac{v\cos\phi - v_{\text{sub}}\cos\theta}{v\sin\phi - v_{\text{sub}}\sin\theta}
\end{aligned}
\qquad (4)
$$

where v_b and ψ denote blood flow absolute velocity and its angle (Fig. 2). Equation (2) can then be modified as

$$u^{\text{sub}}(x,y) = u_s(y) - \int_{x_s}^{x} \partial_y v(x,y)dx \qquad (5)$$

where subscript 's' denotes the boundary condition created with the subbeam. Theoretically, multiple BCs can be created by adding multiple subbeams.

When multiple calculation pathways exist, the final flow velocity is corrected on the basis of VFM velocities calculated using different boundary conditions. When N types of calculations depending on the boundaries along the same integration path exist, for each velocity u_b calculated from boundary condition b, the distance from the boundary to the point of interest is defined as l_b and the following simply weighted function used to calculate the corrected VFM velocities is
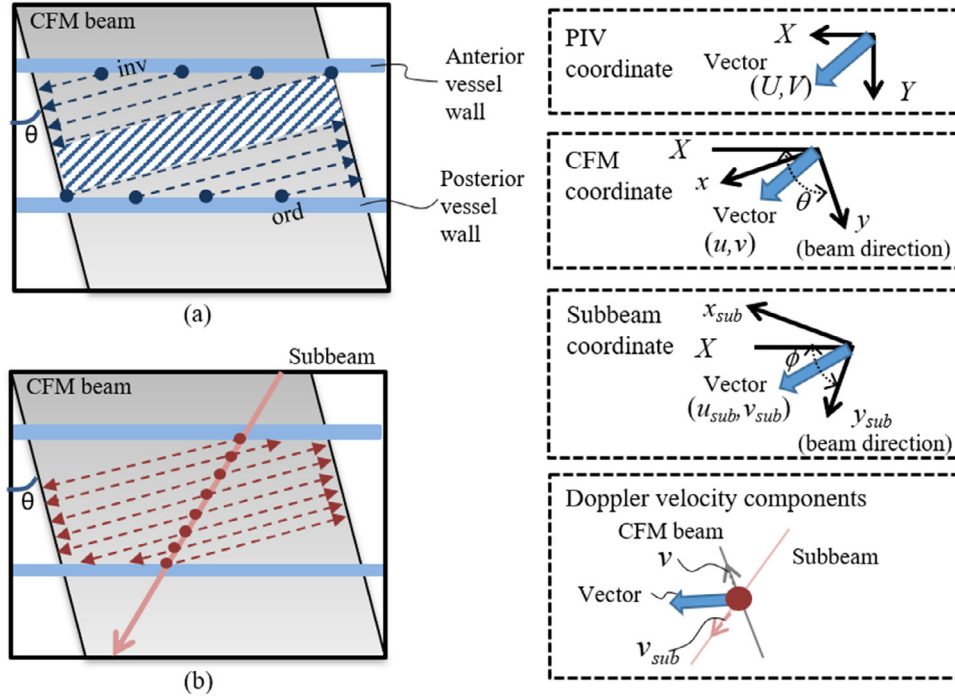
Fig. 1. Vascular VFM algorithm: (a) vascular VFM algorithm using a vessel wall as a boundary condition and (b) alternation to VFM algorithm using subbeam velocity. CFM = color flow mapping; PIV = particle image velocimetry; VFM = vector flow mapping.

$$u^M = \sum_{i=1}^{N} \frac{L - l_{bi}}{L} u_{bi} \qquad (6)$$

where superscript 'M' denotes measured quantities, and L is defined as

$$L = \sum_{i=1}^{N} l_{bi} \qquad (7)$$

METHODS

Carotid artery phantom

A CA phantom was fabricated on the basis of computer-aided design data of the human artery (right carotid artery model, Virtual Anatomia, Japan SGI, Japan) with a
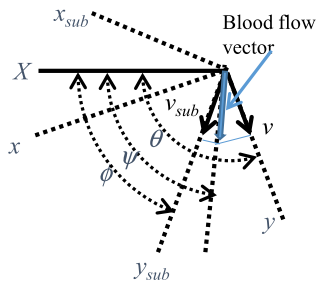

Fig. 2. Vector calculation using two Doppler beams.

thickness of 2 mm (Fig. 3a). The phantom was made of transparent soft urethane resin (Exceal Corp., Japan). The molded phantom was translucent in air (Fig. 3b). The measured refractive index of the phantom was 1.47 (at optical wavelength $\lambda = 532$ nm). The measured density and sound speed of the phantom were 1.02 g/cm^3 and 1391 m/s, respectively, and thus, the acoustic impedance of the phantom was 1425 kg/s/m^2. The base and top of the phantom were fixed to an experimental setup with an acrylic cap.

To eliminate potential optical distortion, reflective indices of the intra-circulatory fluid and external fluid must be matched with that of the silicone rubber used to fabricate the phantom. Polyethylene glycol 400 (PEG400, Wako Pure Chemical Industries, Ltd., Japan), with a refractive index of 1.47 at $\lambda = 532$ nm and viscosity of $6e^{-6}$ m^2/s at room temperature, was selected for this purpose. The measured density and sound speed of PEG400 were 1.13 g/cm^3 and 1610 m/s, respectively, and thus, the acoustic impedance of the phantom was 1819 kg/s/m^2. A trace amount of glass beads (EMB-20, Potters Ballotini Co., Ltd., Japan) with an average diameter of 20 μm were mixed with intra-circulatory fluid for particle image velocimetry (PIV) particle-tracking purposes and as acoustic scatterers.

Experimental setup

The experimental setup is illustrated in Figure 4. The system roughly consists of the CA phantom, a
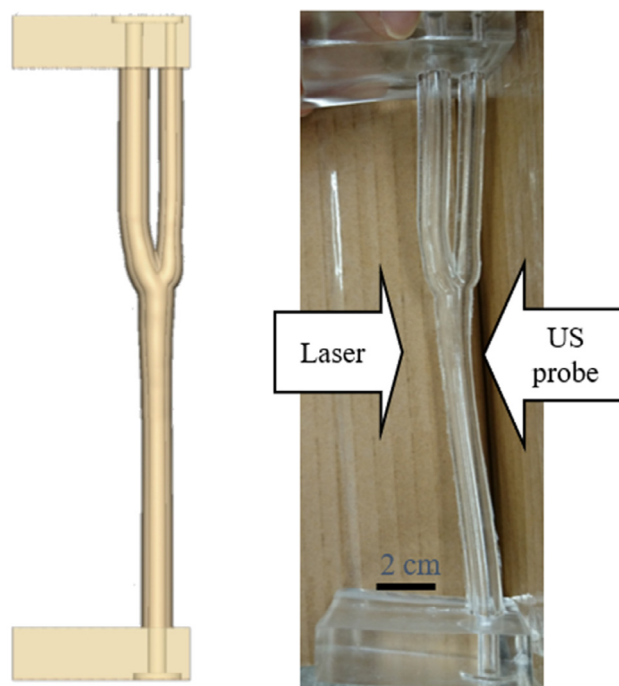
Fig. 3. Carotid artery phantom. (a) Three-dimensional computer-aided design data. (b) Fabricated phantom.
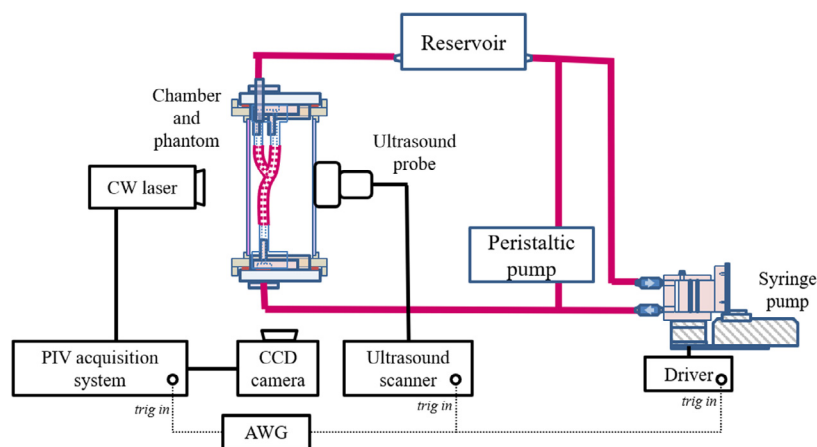

Fig. 4. Experimental setup. AWG = arbitrary wave generator; CW = continuous wave; CCD = charge-coupled device; PIV = particle image velocimetry.

chamber that houses the phantom, a syringe pump, a static-pressure control reservoir, a PIV system and an ultrasound scanner.

The CA phantom was fixed to an acrylic pressurized chamber in the direction that the flow is upward. One side of the chamber consisted of a polymethyl pentene plate that served as an acoustic window for ultrasonic observation, and the opposite side consisted of glass plates that served as an optical window for PIV observation. A flow system consisting of a static-pressure control reservoir, a syringe pump and a peristaltic pump was connected to the phantom. A periodic and pulsatile flow was generated

by an in-house syringe pump (ejecting 44 cm^3 of fluid per stroke) driven with a motor (F14-10, Yamaha Motor Co., Ltd., Japan) connected to the chamber. A peristaltic pump (7518-12, Cole-Parmer Instrument Co., LLC, USA) was also connected to assist the flow.

The PIV system consisted of a camera (Speed-Sense1010, Dantec Dynamics, A/S, Denmark), a continuous wave Nd:YAG laser with maximum output of 5 W (Raypower 5000, Dantec Dynamics, Denmark) and control and analysis software (Dynamic Studio V3.31, Dantec Dynamics, A/S, Denmark). The second-harmonic wavelength (532 nm) was used to create a green laser

sheet with a thickness of approximately 1 mm in the field of view. The optically imaged data were acquired at a 500 Hz frame rate, and the shutter speed of the camera was set at 300 μs.

A linear probe (UST-5415, Hitachi Aloka Medical, Ltd., Japan) connected to a clinical ultrasound scanner (ProSound F75, Hitachi Aloka Medical, Ltd., Japan) was placed at the bottom of the pressurized chamber. The probe was precisely positioned to visualize the plane illuminated by the laser sheet. Data from a B-mode image and color Doppler (CFM) were acquired with a center frequency of 5 MHz. The CFM steering angle was adjusted from 5° to 20°. Frame rate was varied from 11 to 13 Hz according to steering angle. As the steering angle becomes greater, the width of the region of interest becomes smaller and the number of beamlines required decreases. CFM dynamic range was set at the lowest possible velocity with no sign of aliasing. Because of the difference in the speeds of sound in tissue and PEG400, the default speed of sound was adjusted to 1610 m/s from the original setting of 1530 m/s. The location of the subbeam was determined according to the steering angle of the CFM beams and number of subbeams so as to maximize the number of calculation pathways resulting from the created boundary conditions. The same parameters (such as the number of packets used) used for the subbeam were used for the CFM beam. Beam sequence was modified so that a subbeam transmit/receive sequence was inserted after the CFM transmit/receive sequence had been repeated for all scan lines. To compare the VFM and PIV vectors, the same calibration board was used to unify the coordinate system.

An arbitrary wave generator (33220A, Agilent Technologies, Inc., USA) was connected to the syringe pump, ultrasound scanner and PIV controller to synchronize the phantom motion with VFM data acquisition and the PIV camera frame trigger given at 1 Hz.

Analysis of PIV data

The background was removed from the acquired PIV image by subtracting the reference frame acquired at the same timing after the trigger pulse. Velocity maps with an interrogation size of 32×8 pixels (with 75% overlaps in each direction) were then generated, thereby providing a spatial resolution of approximately 0.68×0.17 mm. Velocities U and V represent velocities measured by PIV in the X and Y directions, respectively, as illustrated in Figure 1.

Analysis of vascular VFM data

To prepare the data for VFM analysis, radiofrequency data from color Doppler echocardiography were analyzed offline using DAS-RS1 software (Hitachi Aloka Medical, Ltd., Japan). The vessel wall was manually traced in a diastolic frame and automatically traced for all frames by using the pyramidal Kanade−Lucas−Tomasi tracker method (Kusunose et al. 2014). Tissue velocities were calculated, and then neighboring vectors were averaged. CFM data were preliminarily filtered in the depth and transverse directions by using an averaging filter before the VFM was calculated. The vascular VFM algorithm (as detailed in the previous section) was
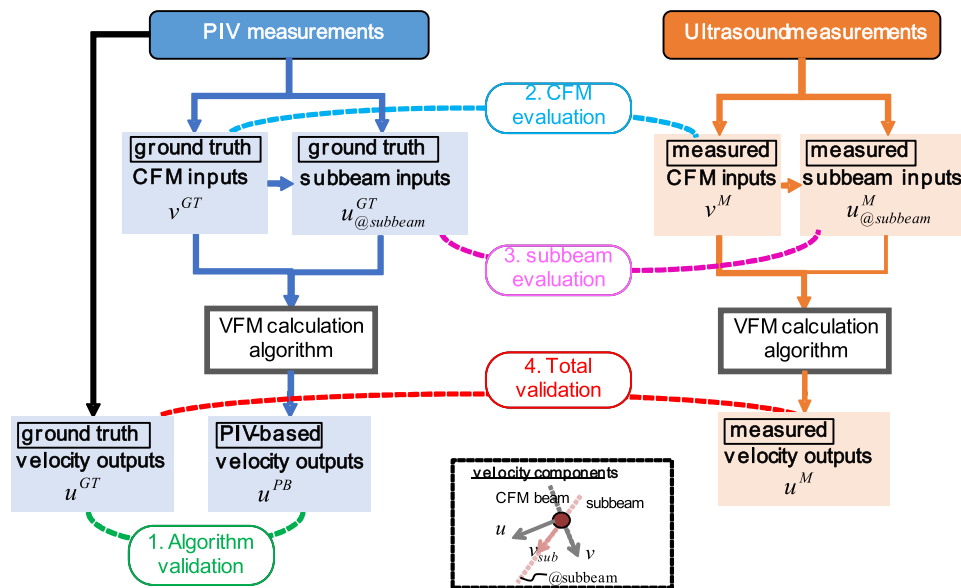

Fig. 5. Comprehensive validation schemes for VFM. CFM = color flow mapping; PIV = particle image velocimetry; VFM = vector flow mapping.

developed using MATLAB (The MathWorks, Inc., Natick, MA, USA). Wall velocity was determined by manually tracing the internal surfaces of walls and registering images using a fast method of cross-correlation (Guizar-Sicairos et al. 2008) to track wall displacement.

Validation of vascular VFM

A general validation protocol called the "comprehensive validation scheme" for investigating the accuracy in each step of the calculation process (*i.e.,* accuracy of measured inputs, of algorithm with ideal inputs and of total output with measured inputs) is proposed. Specifically, vascular VFM was validated from the four aspects (as shown in Fig. 5): (i) VFM algorithm based on mass conservation; (ii) CFM input data accuracy; (iii) subbeam accuracy; and (iv) total accuracy. The validation was conducted for the common CA tract of the phantom.

To evaluate the VFM algorithm itself, setting aside for the moment the accuracy of the input-flow measurements, the algorithm was applied to the ground truth PIV data. Briefly, the data were prepared by resampling both temporally and spatially and recalculating PIV vectors (Fig. 6a) to make ground truth (GT) CFM and subbeam velocity inputs (*yellow and green vectors*, respectively, in Fig. 6b). The region of interest was set at an arbitrary steering angle of the CFM beam and PIV vectors inside the region re-sampled to color Doppler sampling size, namely, 0.038 mm in the depth direction and 0.6 mm in the transverse direction. From the PIV vectors, GT depth directional velocity projected in the Doppler beam direction (*i.e.,* CFM velocity), v^{GT}, and transverse directional velocity, u^{GT}, were calculated. Subbeam Doppler velocity, v^{GT}_{sub}, and transverse velocity along the subbeam, $u^{GT}_{@subbeam}$ (where subscript "@subbeam" denotes the components along the subbeam), were also calculated in the same manner. The calculated ground truth velocities with wall velocities obtained by PIV tissue tracking were input to the vascular VFM algorithm. The calculated velocity is defined as "PIV-based" transverse velocity, u^{PB}, and was compared with the ground-truth transverse velocity, u^{GT}.

As illustrated in Figure 5, a CFM evaluation quantified the measured CFM accuracy by comparing the measured CFM velocity, v^M, and the ground truth velocity, v^{GT}, calculated by using the PIV data sets at a steering angle ranging from 5° to 20°. Superscript 'M' denotes "measured" quantities. Dependence of the accuracy of CFM measurements on steering angle was also investigated.

Similarly, the subbeam evaluation quantified the accuracy of the boundary condition, or the vector calculation, as the VFM algorithm set the third boundary condition by calculating the velocity vector from CFM and subbeam Doppler velocities. The vector measured as a boundary condition in the CFM transverse direction, $u^M_{@subbeam}$, was compared with ground-truth velocity $u^{GT}_{@subbeam}$ obtained by PIV. Dependence of the accuracy on steering angle was also investigated.

On the basis of eqn (4), error tolerances of the vector calculation (which depend on steering angle) were simulated in MATLAB. For the simulation conditions, $v = 1$, $v_{sub} = 1$, $\phi = 5°$ to 25° and $\theta = -5°$ to $-25°$ were used to evaluate the propagated vector error when input velocity v had a 5% error.

The accuracy of the total calculation of VFM velocity (including both measurement accuracy and algorithm accuracy) was validated. Dependency of the accuracy of transverse velocity u^M on steering angle was investigated by comparing it with ground truth velocity u^{GT}.

RESULTS

Qualitative evaluation of flow

The time course of PIV and CFM velocity illustrated in Figure 7 confirms that a pulsatile flow at 1 Hz was re-created in the phantom setup. Maximum flow speed immediately before the branch of the phantom is approximately 52 cm/s, which is comparable to that of healthy adults. This maximal velocity is used to normalize standard deviations (SDs) in later sections. CFM velocity is acquired at beam angle of 10° relative to the flow, and the velocity is slightly underestimated because of spatial averaging. Both the proximal and distal wall of the phantom slightly expanded at an average wall
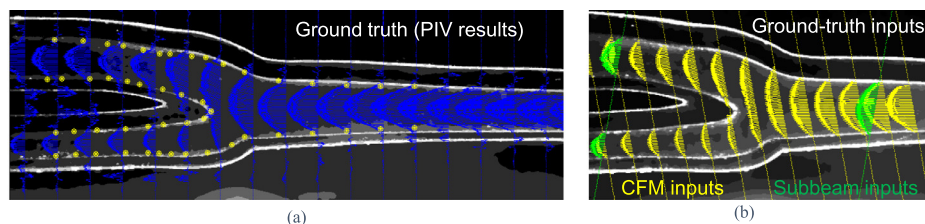

(a)   (b)

Fig. 6. Procedure for processing PIV data: (a) velocity mapping of PIV data and (b) resampling Doppler vectors (yellow) and subbeam vectors (green) from acquired PIV data. CFM = color flow mapping; PIV = particle image velocimetry.
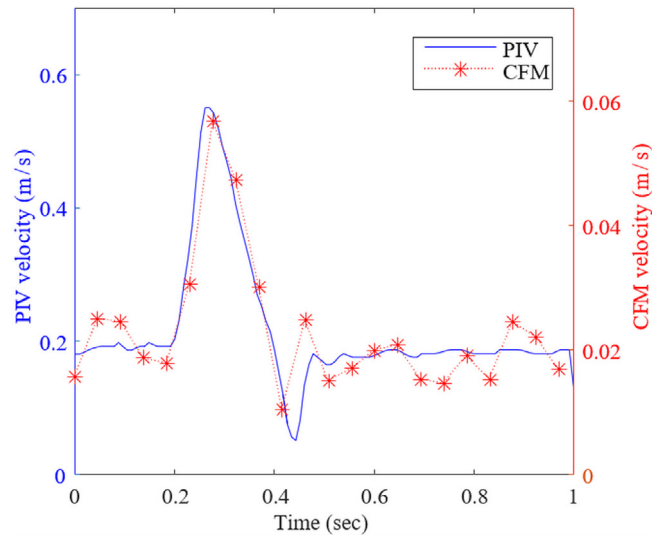
Fig. 7. Time course velocity plot of PIV and CFM data. Data were acquired at the middle of the common carotid tract of the arterial phantom, where the flow was at maximum within the CFM imaging plane. CFM velocity was acquired at a beam angle of 10° relative to the flow. CFM = color flow mapping; PIV = particle image velocimetry.

expansion of 5% over the phantom diameter in the straight vessel part.

Vector maps for the common carotid tract and for the bifurcation are provided in Figure 8(a, b) and 8(c, d), respectively. The ground-truth vectors obtained by PIV are provided in Figures 8(a, c), and the VFM vectors, in Figure 8(b, d). The vectors are overlaid on gray-scale images. Two subbeams were used to calculate vascular

VFM vectors. The VFM results (Fig. 8b, d) reveal vector fields similar to those for ground truth. Further validations are given as follows.

Validation of vascular VFM algorithm with ideal input
The algorithm validation (in Fig. 5) was conducted to quantify the accuracy of the algorithm itself. In Figure 9 are velocity maps for (a) PIV-based and (b)
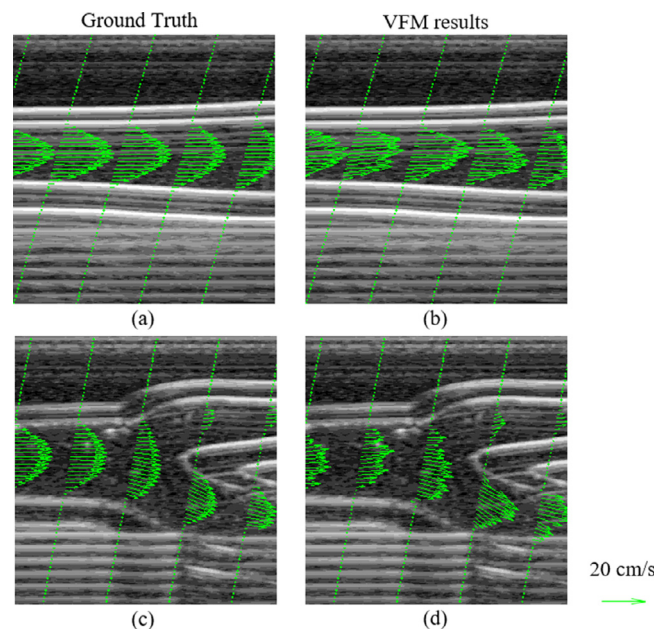

Fig. 8. Vector maps for (a, b) the common carotid tract and (c, d) the bifurcation of the arterial phantom immediately after the systolic phase. Ground-truth vectors obtained by particle image velocimetry are illustrated in (a) and (c), and VFM results, in (b) and (d). A sale vector refers to full velocity. VFM = vector flow mapping.
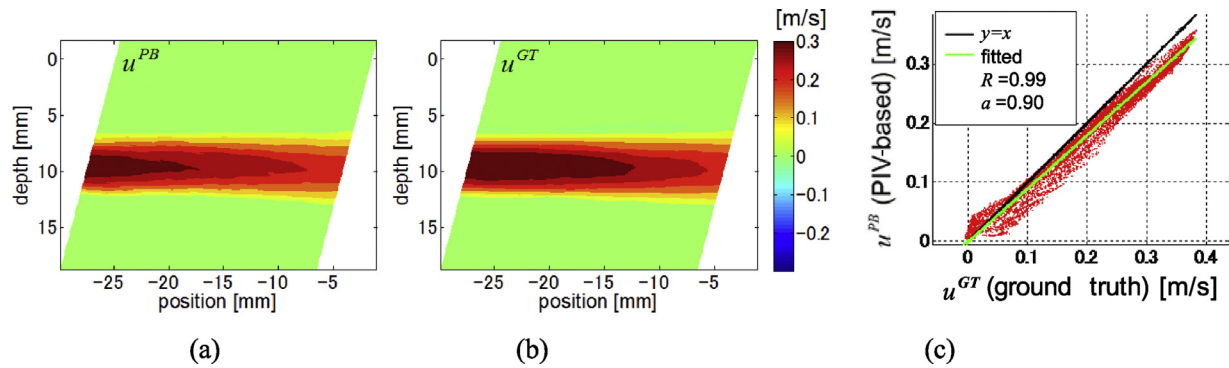
Fig. 9. Velocity maps for (a) PIV-based velocity output, (b) ground-truth velocity output, (c) correlation between PIV-based and ground-truth velocities for a straight vessel under an assumed color flow mapping steering angle of 15° and subbeam steering angle of −10°. In (a) and (b), horizontal position is set at zero at where the phantom branches out. The velocities were measured immediately after the systolic phase. PIV = particle image velocimetry.

ground truth velocity outputs for the the common carotid tract of the arterial phantom, which is also referred to as a straight vessels (under the assumption of a CFM steering angle of 15° and subbeam steering angle of −10°, with one subbeam used for the calculation). Quantitatively, the SD of error in the particular frame in this figure is 2.7% of maximum flow speed, 52 cm/s. The correlation between u^{PB} and u^{GT} illustrated in Figure 9c for straight vessels is excellent, namely, $R = 0.99$.

The correlation between PIV-based velocity and ground truth velocity, where data were categorized according to the number of BCs, is illustrated in Figure 10a. The color of the plots indicates the number of boundary conditions. With increasing number of BCs, the correlation strengthens. The relationship between error magnitude and number of BCs is illustrated in Figure 10b. With increasing number of boundary conditions, the error decreases. At least two BCs suppress the error effectively. In Figure 10c are contour plots of calculation errors normalized by maximum velocities for all experimental conditions. The SD of the error ranges from 1.9% to 4.3%. As CFM beam angle increases, the error increases.

Evaluation of CFM and subbeam boundary conditions

The CFM validation scheme illustrated in Figure 5 was conducted to estimate the accuracy and precision of input CFM used in the present study. The correlation between measured CFM velocity, v^M, and ground truth velocity, v^{GT}, for straight vessels (under an assumed CFM steering angle of 15° and subbeam steering angle of −10°) is provided in Figure 11a. The correlation coefficient R of 0.97 reflects excellent agreement. Dependence of evaluated CFM precision (*i.e.,* SD) on steering angle (from 5° to 20°) for straight vessels as a typical common artery is plotted in Figure 11b. The error was

normalized by maximum ground truth velocity in the beam direction. For smaller steering angle, the error of the CFM dramatically increases, as the Doppler measurement is accurate when the flow direction and the ultrasound beam direction are almost parallel. In particular, the SD of the error reaches 26% at 5°, but decreases to 8.9% at 20°.

The accuracy of the subbeam calculation employed in determining the BCs used in the VFM integrations was evaluated as follows. The correlation between the measured subbeam boundary condition, $u^M_{@subbeam}$, and its GT, $u^{GT}_{@subbeam}$, for straight vessels (under an assumed CFM steering angle of 15° and subbeam steering angle of −10°) is illustrated in Figure 12a. A correlation coefficient R of 0.93 and SD of the error of 5.9% indicate that the accuracy of the subbeam calculation is high. For the other CFM steering angle and subbeam steering angle conditions, the SD of the error ranges from 4.5% to 5.9%.

Angle dependency of the vector calculation was investigated by using a simple simulation. Error propagation was simulated for various subbeam angle φ and CFM steering angle conditions, given the CFM has a 5% error and one subbeam is used as a boundary condition (Fig. 12b). The larger the angle between the two beams, the smaller the calculation error becomes.

Total validation of vascular VFM

The vascular VFM (including algorithm and input accuracies) was validated in total (as illustrated in Fig. 5). Velocity maps for (a) measured VFM velocity, u^M, and (b) ground truth velocity, u^{GT}, for straight vessels under an assumed CFM steering angle of 15° and subbeam steering angle of −10° are provided in Figure 13. Compared with the ground truth, the measured VFM velocity map has stripes derived from the integration path. Quantitatively, in this particular frame,
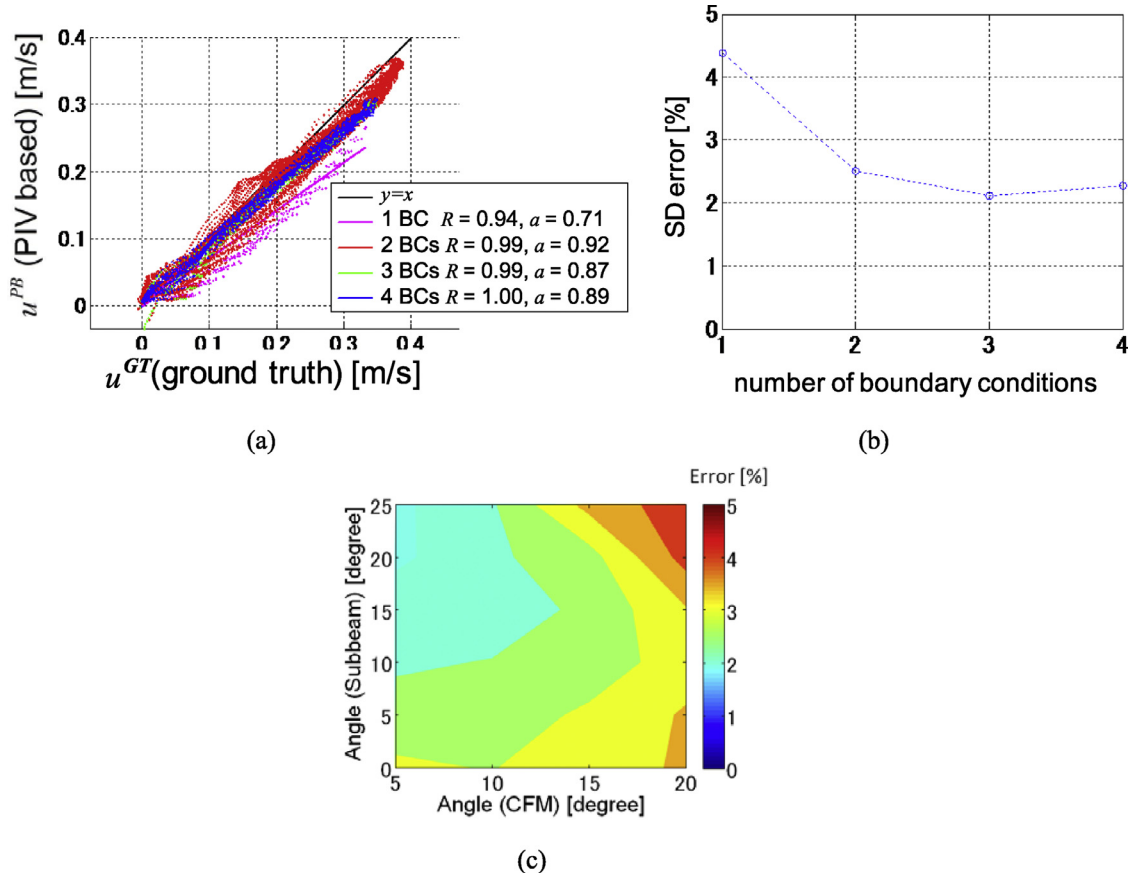
Fig. 10. Accuracy of vascular vector flow mapping algorithm. (a) Relationship between distance from the closest boundary and calculation errors. (b) Relationship between number of boundaries and accuracy. (c) Dependence of error (%) of estimated velocity on beam angle. BC = boundary condition; CFM = color flow mapping; PIV = particle image velocimetry; SD = standard deviation.

the SD is 2.8% of maximum flow speed. The correlation between u^M and u^{GT} illustrated in Figure 9c for straight vessels is excellent; namely, $R = 0.95$.

Contour plots of the SD of the error of velocity, normalized by the maximum speed, depending on both CFM beam angle and subbeam angle, are provided in Figure 14. The errors for all experimental conditions used in the present study are in the range 8.1% to 19.8%. For a larger CFM steering angle, namely, that ranging from 10° to 20°, the error drops to less than 16.3%.
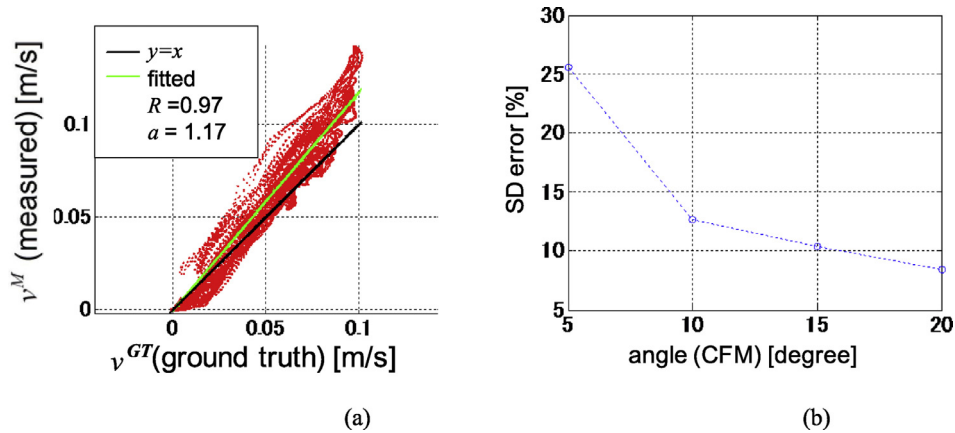

Fig. 11. (a) Error in correlation between measured velocity and ground-truth CFM velocity at steering angle of 15°. (b) Dependence of CFM error on steering angle. CFM = color flow mapping; SD = standard deviation.
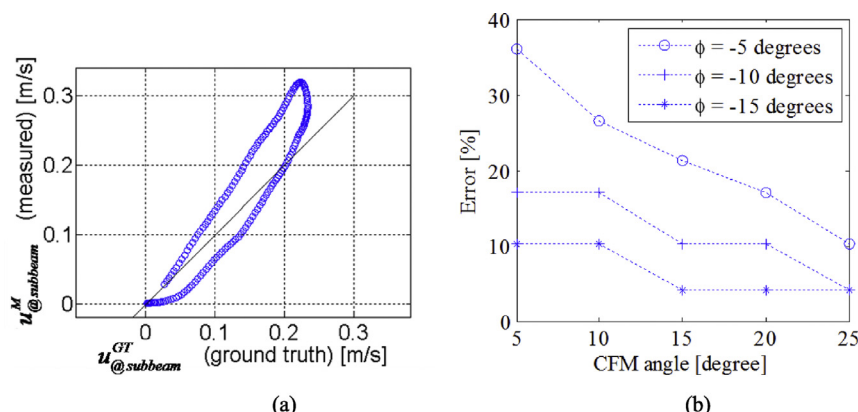
Fig. 12. Accuracy of vector calculation. (a) Correlation between calculated subbeam velocities and their ground truth for straight vessels under assumed CFM steering angle of 15° and subbeam steering angle of −10°. (b) Scatterplot revealing error propagation of subbeam boundary conditions. The calculated vector error for an input velocity (v) error of 5 % was calculated for simulation conditions $v = 1$ and $v_{sub} = 1$. CFM = color flow mapping.

DISCUSSION

In this work, we have proposed a vascular VFM algorithm and validated it using PIV data. The VFM algorithm error is less than 5% given PIV inputs for the CFM beam and subbeams, namely, a steering angle ranging from 10° to 20°. The subbeam calculation of the SD of the error is approximately 5%, and that for CFM is around 10%, resulting in a total VFM error ranging from 8% to 16% (as illustrated in Fig. 14).

The results of the validation suggest that vascular flow can be accurately estimated using the mass conservation equation assuming planar flow, given that the input variables, namely, Doppler velocity and wall velocities, are accurately measured. The majority of the VFM algorithm error (3% of the 5% total) seems to depend on the number of BCs (Fig. 10a). The error was suppressed when the number of BCs was ≥2 (Fig. 10b) because the error reduction shown in eqn (4) effectively works in the case of multiple boundary conditions. The error increases with increasing

steering angle because of the geometric relationship of the subbeams. That is, to maximize the number of calculation pathways, the two subbeams are positioned so that they always pass through the opposing vertices of the CFM region of interest.

The limitation of the algorithm is, obviously, the planar flow assumption. This study was conducted in an ideal scenario where the vessel was not stenotic. In cases where the vessel *is* stenotic, flow can become helical/turbulent and the planar flow assumption would be challenged, resulting in a VFM accuracy that could be significantly lower than presented here. The previous study on accuracy of the VFM method in the left ventricular phantom, in which flow three-dimensional flow is present, reports that the standard deviation of discrepancy is 10% over CFM velocity range at the maximum (Asami et al. 2017). In the presence of 3-D flow, the previously proposed uncertainty estimation could be employed to provide the user with an estimate of VFM accuracy (Tanaka et al. 2017).
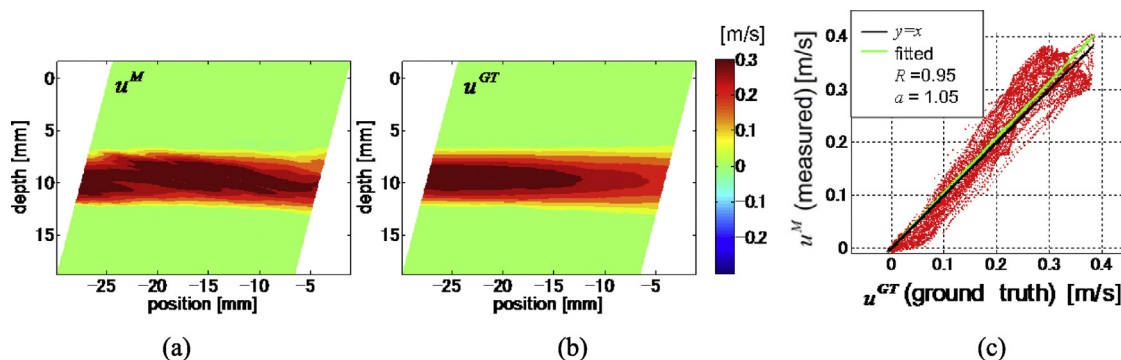

Fig. 13. Velocity maps for (a) vector flow mapping velocity output, u^M, (b) ground-truth velocity output, u^{GT}, and (c) correlation between PIV-based and ground-truth velocities for straight vessels under assumed CFM steering angle of 15° and subbeam steering angle of −10°.
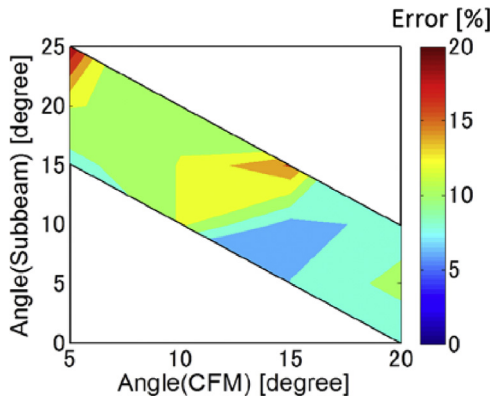
Fig. 14. Contour plots of estimated velocity, u^M, standard deviation of the error depending on beam angle. CFM = color flow mapping.

Many vector flow imaging techniques have been reported to date (Jensen et al. 2016). The advantage of this method is it only requires one to three lines of additional transmission of subbeams to conventional CFM. This means that the frame rate would not decrease significantly and that the method can be easily implemented in a readily available ultrasound scanner. The algorithm proposed here has the same limitation as conventional VFM. For example, CFM aliasing has to be corrected, and the wall filtering has to be minimized to correctly evaluate the vectors. These are disadvantages of other non-CFM-based vector flow imaging methods.

The optimal conditon in terms of CFM steering angle for the horizontal flow direction (such as in the general CA) is $>5°$ (Fig. 14). This condition can be defined as the optimal condition. As illustrated in Figure 11a, the correlation between Doppler velocity components of GT and measured CFM velocity indicates that measured CFM velocity is reasonably accurate ($R = 0.97$). The CFM evaluation for straight vessels (mimicking a common CA) revealed that CFM accuracy decreases for small beam angles such as 5° when the artery is horizontal (Fig. 11b). This represents a marked decrease in CFM accuracy for cases in which the streering angle is $<10°$, as the Doppler signals can hardly be captured when the beam is closely normal to the flow direction. The CFM evaluation yielded the typical CFM accuracy under optimal conditions of approximately 10%. It is thus suggested that the angle between the CFM beam and the artery should be $<85°$ degrees for vascular VFM.

When practically setting the imaging conditions, several constrains (such as flow angle, depth and geometry) are involved. To perform VFM accurately, the beam angle should be set as large as possible within the constraints, where each beam is set normal to the flow direction, as the error propagation analysis (Fig. 12b) for the boundary condition calculation indicates that a large beam angle between the CFM beam and subbeam suppresses the calculation error.

With two subbeams as boundary conditions, vascular VFM could estimate velocities over the entire region of interest, and the overall flow pattern of VFM agreed well with the PIV measurements. Because the vascular VFM algorithm itself has proved to yield a much smaller margin of error, as detailed in the previous section, it is suggested that this error is caused by the low quality of CFM, subbeam and wall-tracking data. Errors in CFM measurements directly result in errors in the BCs provided by the subbeams. It should be noted that the boundary condition created at the intersection between the subbeam and the CFM beam is assumed to have a certainty comparable to that of the BCs at vascular walls. Although this assumption holds true in the case of PIV, it is challanged in the case of echography. Wall motion is derived from tissue tracking using a B-mode image, whereas flow velocities are based on CFM beam data, which is different in terms of spatial resolution and signal sensitivity.

In this study, PIV data were treated as GT, as measurement of 2-D flow field optically is an accepted method. Our previous study confirmed that the PIV-measured experimental velocity distribution agreed with the analytical result with a mean error of -2.3% (Shimizu et al. 2017). Our phantom created a resonable flow for the purpose of accuracy validation. It should be noted that although the phantom is created to mimic the size and shape of a human CA, the viscosity of inter-circulatory fluid is about 1.5 times higher than that of the blood at 37°C, resulting in an unmatched Reynold's number. However, this limitation does not affect the findings of the current study, because turbulant flow was not considered in this study. We should also point out that the difference in acoustic impedance between polyethylene glycol 400 and phantom material is larger than what is expected between blood vessel wall and blood, and causes larger scattering at vessel walls. Although excessive scattering could interfere with CFM and B-mode images in the form of acoustic shadowing, that was not the case in this study.

A certain margin of error is allowed in clinical applications, and in vascular applications, 15% is assumed to be within that margin. One of the most important hemodynamic parameters derived from 2-D vectors in vascular flow is wall shear stress. Its clinical impact relies on differentiating a high-shear-stress region from a low-shear-stress region, which requires a resolution of approximatory 0.5 Pa (Nishiyama and Katakura 1992; Yatchenko et al. 2014). To reach the desired resolution, derivatives of vascular VFM-estimated velocity are curve-fitted to estimate wall shear stress, and the fitting error is within 15 cm/s. As the

maximal flow speed in carotid arteries is approximately 1 m/s, vascular VFM could be a valid clinical tool for determining wall shear stress.

CONCLUSIONS

Vascular VFM with a novel beam sequence to visualize 2-D flows in vascular applications was proposed, and its accuracy was validated using an *in vitro* phantom mimicking the human CA. The phantom was made to be optically and acoustically measurable in the same image plane so that PIV velocity fields can be compared with those obtained by VFM. For vascular VFM, the optimized CFM beam angle and subbeam angles range from 10° to 20°. In addition, there should be multiple BCs along an integration path. Under these optimal conditions, the SD of the total VFM error, normalized by maximum velocity, is reasonably small, that is, 8.1%−16.3%, where the SD of the measured input errors ranges from 8.9% to 12.7% for CFM and from 4.5% to 5.9% for subbeam calculation. Moreover, the SD of the VFM algorithm error with ideal inputs ranges from 1.9% to 4.3%. The results presented here indicate that vascular VFM is comparable to conventional Doppler flow measurements in terms of accuracy and could be clinically significant.

REFERENCES

Asami R, Tanaka T, Kawabata K-i, Hashiba K, Okada T, Nishiyama T. Accuracy and limitations of vector flow mapping: Left ventricular phantom validation using stereo particle image velocimetory. J Echocardiogr 2017;15:57–66.

Fox MD. Multiple crossed-beam ultrasound Doppler velocimetry. IEEE Trans Sonics Ultrason 1978;25:281–286.

Garcia D, Del Alamo JC, Tanne D, Yotti R, Cortina C, Bertrand E, Antoranz JC, Perez-David E, Rieu R, Fernandez-Aviles F, Bermejo J. Two-dimensional intraventricular flow mapping by digital processing conventional color-Doppler echocardiography images. IEEE Trans Med Imaging 2010;29:1701–1713.

Gimbrone MA, Jr, Garcia-Cardena G. Vascular endothelium, hemodynamics, and the pathobiology of atherosclerosis. Cardiovasc Pathol 2013;22:9–15.

Guizar-Sicairos M, Thurman ST, Fienup JR. Efficient subpixel image registration algorithms. Opt Lett 2008;33:156–158.

Itatani K, Okada T, Uejima T, Tanaka T, Ono M, Miyaji K, Takenaka K. Intraventricular flow velocity vector visualization based on the continuity equation and measurements of vorticity and wall shear stress. Jpn J Appl Phys 2013;52 07HF16-1-13.

Jensen JA, Nikolov SI, Yu ACH, Garcia D. Ultrasound vector flow imaging—Part I. Sequential systems. IEEE Trans Ultrason Ferroelectr Freq Control 2016;63:1704–1721.

Kim HB, Hertzberg JR, Shandas R. Development and validation of echo PIV. Exp Fluids 2004;36:455–462.

Kusunose K, Chono T, Tabata T, Yamada H, Sata M. Echocardiographic image tracker with a speckle adaptive noise reduction filter for the automatic measurement of the left atrial volume curve. Eur Heart J Cardiovasc Imaging 2014;15:509–514.

Muth S, Dort S, Sebag IA, Blais MJ, Garcia D. Unsupervised dealiasing and denoising of color-Doppler data. Med Image Anal 2011; 15:577–588.

Namekawa K, Kasai C, Tsukamoto M, Koyano A. Realtime bloodflow imaging system utilizing auto-correlation techniques. Ultrasound Med Biol 1983;2(Suppl):203–208.

Nishiyama H, Katakura K. Non-equally-spaced pulse transmission for non-aliasing ultrasonic pulsed Doppler measurement. J Acoust Soc Japan (E) 1992;13:215–222.

Nogami Y, Ishizu T, Atsumi A, Yamamoto M, Kawamura R, Seo Y, Aonuma K. Abnormal early diastolic intraventricular flow 'kinetic energy index' assessed by vector flow mapping in patients with elevated filling pressure. Eur Heart J Cardiovasc Imaging 2013; 14:253–260.

Ohtsuki S, Tanaka M. The flow velocity distribution from the doppler information on a plane in three-dimensional flow. J Visualization 2006;9:69–82.

Posada D, Poree J, Pellissier A, Chayer B, Tournoux F, Cloutier G, Garcia D. Staggered multiple-PRF ultrafast color Doppler. IEEE Trans Med Imaging 2016;35:1510–1521.

Ridger V, Krams R, Carpi A, Evans PC. Hemodynamic parameters regulating vascular inflammation and atherosclerosis: A brief update. Biomed Pharmacother 2008;62:536–540.

Ro R, Halpern D, Sahn DJ, Homel P, Arabadjian M, Lopresto C, Sherrid MV. Vector flow mapping in obstructive hypertrophic cardiomyopathy to assess the relationship of early systolic left ventricular flow and the mitral valve. J Am Coll Cardiol 2014;64:1984–1995.

Sengupta PP, Pedrizzetti G, Kilner PJ, Kheradvar A, Ebbers T, Tonti G, Fraser AG, Narula J. Emerging trends in CV flow visualization. JACC Cardiovasc Imaging 2012;5:305–316.

Shimizu M, Tanaka T, Okada T, Seki Y, Nishiyama T. Wall shear stress measurement method based on parallel flow model near vascular wall in echography. Jpn J Appl Phys 2017;56 07JF08.

Tanaka T, Asami R, Kawabata KI, Hashiba K, Okada T. Method for estimating uncertainty in individual vector-flow-mapping measurements. In: Proc IEEE Int Ultrason Symp 315–318.

Tanaka T, Asami R, Kawabata K, Hashiba K, Okada T, Nishiyama T. A posteriori accuracy estimation of ultrasonic vector-flow mapping (VFM). J Vis 2017;20:607–623.

Uejima T, Koike A, Sawada H, Aizawa T, Ohtsuki S, Tanaka M, Furukawa T, Fraser AG. A new echocardiographic method for identifying vortex flow in the left ventricle: Numerical validation. Ultrasound Med Biol 2010;36:772–788.

Yatchenko AM, Krylov AS, Sandrikov VA, Kulagina TY. Regularizing method for phase antialiasing in color Doppler flow mapping. Neurocomputing 2014;139:77–83.